Tuning Work Function of Fe2N@C Nanosheets by Co Doping for Enhanced Lithium Storage

Peer-reviewed author version

Chen, Yifan; Huang, Qiang; Zhao, Rong; Sun, Bing; Xu, Wenli; Gao, Yinhong; Nan, Xu; Li , Qiqi; Yang , Yao; Cong, Ye; Li, Xuanke; Zhang, Qin & YANG, Nianjun (2024)
Tuning Work Function of Fe2N@C Nanosheets by Co Doping for Enhanced Lithium Storage. In: Small,.

DOI: 10.1002/smll.202405608
Handle: http://hdl.handle.net/1942/44607

DOI: 10.1002/((please add manuscript number))

Article type: Communication

Tuning work function of Fe_2N@C nanosheets by Co doping for enhanced lithium storage

Yifan Chen[#,1], Qiang Huang[#,1], Rong Zhao[1], Bing Sun[3], Wenli Xu[1], Yinhong Gao[1], Xu Nan[1], Qiqi Li[1], Yao Yang[1], Ye Cong[1], Xuanke Li[1], Qin Zhang[,1], and Nianjun Yang*[,2]*

[1] Hubei Province Key Laboratory of Coal Conversion and New Carbon Materials, School of Chemistry and Chemical Engineering, Wuhan University of Science and Technology, Wuhan 430081, China
E-mail: zhangqin627@wust.edu.cn (Qin Zhang)

[2] Department of Chemistry, Hasselt University, Agoralaan 1 - Buidling D, 3590 Diepenbeek, Belgium IMO-IMOMEC, Hasselt University, Wetenschapspark 1, 3590 Diepenbeek, Belgium
E-mail：nianjun.yang@uhasselt.be

[3] Key Laboratory of Inorganic Nonmetallic Crystalline and Energy Conversion Materials, College of Materials and Chemical Engineering, China Three Gorges University, Yichang, 443002, China

[#] These authors contributed equally to this manuscript.

Abstract: Transition metal nitrides (TMNs) with high theoretical capacity and excellent electrical conductivity have great potential as anode materials for lithium-ion batteries (LIBs), but suffer from poor rate performance due to the slow kinetics. Herein, taking the Fe_2N for instance, Co doping is utilized to enhance the work function of Fe_2N, which accelerates the charge transfer and strengthens the adsorption of Li^+ ions. The Fe_2N nanoparticles with various Co dopants are anchoring on the surface of honeycomb porous carbon foam (named Co_x-Fe_2N@C). Co-doping can enlarge the work function of pristine Fe_2N and thereby optimize the

charging/discharging kinetics. The work function can be increased from 5.23 eV (pristine Fe_2N) to 5.67 eV for $Co_{0.3}$-Fe_2N@C and 5.56 eV for $Co_{0.1}$-Fe_2N@C. As expected, the $Co_{0.1}$-Fe_2N@C electrode exhibits the highest specific capacity (673 mA h g^{-1} at 100 mA g^{-1}) and remarkable rate capability (375 mA h g^{-1} at 5000 mA g^{-1}), outperforming most reported TMNs electrodes. Therefore, this work provides a promising strategy to design and regulate anode materials for high-performance and even commercially available LIBs.

Key words: Co doping; iron nitride; work function; optimized kinetics; lithium-ion batteries

Introduction

Lithium-ion batteries (LIBs) have always dominated the power supply market for portable electronic devices and electric vehicles, due to the advantages of long cycle life, high power density, large capacity, high energy efficiency, and low self-discharge properties[1, 2]. The electrode materials determine the energy density and capacity as the most important component in LIBs[3]. Among the emerging anode materials, transition metal nitrides (TMNs) have aroused increasing interest for their excellent electrochemical performance and high chemical stability[4-8]. The coexistence of covalent bonds, ionic bonds, and metal bonds in TMNs makes it exhibit excellent lithium storage performance[9]. Comparing various TMNs that have been reported, Fe_2N is outstanding in both the theoretical capacity and the actual capacity[10]. Fe is one of the most abundant elements in transition metals[11], so its low cost and easy availability make itself a promising material for constructing a LIB anode with high specific capacity, high rate, and stable cycle. Furthermore, the specific electronic configuration of Fe_2N is characterized by the fact that valence electrons can occupy part of the *d* orbital, which means that multivalent states are created to store energy effectively when Fe_2N participates in the redox reaction[12, 13]. The theoretical capacity of Fe_2N (900 mA h g^{-1}) is higher than that of graphite (372 mA h g^{-1}), which is mainly due to the two or three electron transfer reactions that occur when it acts as an anode electrode[14].

Nevertheless, the iron nitrides working as active material are still far from practical application due to their slow kinetics and large volume change during the charge and discharge cycles, which results in fast capacity decay and poor rate performance[15]. To overcome these problems, reducing the size of active materials to nanoscale or compositing with carbon is commonly utilized to facilitate the kinetics and thereby improve the lithium storage performance[16, 17]. For example, hierarchical core-shell Fe_2N nanoparticles are anchored on N-doped carbon nanofiber bundles to buffer the excessive volume change[18]. The Fe_2N hollow nanofibers were successfully obtained via reduction and nitridation, which demonstrates

excellent lithium storage performance[19]. However, a simple nanostructural design or carbon coating cannot fully ensure the rate performance and structural stability during repeated lithiation/delithiation[20, 21]. Doping can change the lattice spacing of the material, thereby adjusting the work function of the material, optimizing the adsorption energy of lithium ions, accelerating the charge transfer, and thus improving the performance of the negative electrode material.

Herein, Co-doping is developed to modulate the work function of a model Fe_2N, thereby accelerating the charge transfer and strengthening the adsorption of Li^+ ions, in turn, giving rise to optimized kinetics of Fe_2N. Co-doping can also increase active sites and improve the conductivity of Fe_2N, as well as be conducive to the pseudocapacitance contribution. The Fe_2N nanoparticles with varying Co-doped contents are well-dispersed and uniformly anchored on the surface of honeycomb N-doped carbon foam (Co_x-Fe_2N@C). The three-dimensional honeycomb carbon foam can effectively increase the specific surface area and conductivity, where the Fe_2N nanoparticles can be uniformly dispersed on the surface to reduce aggregation. Meanwhile, this structure can leave space for volume expansion and contribute to the better infiltration of electroyte. Measured by ultraviolet photoelectron spectroscopy (UPS), the work function of the Fe_2N increases from 5.23 eV to 5.56 eV after Co doping, which matches well with the calculation results. As expected, the resulting $Co_{0.1}$-Fe_2N@C anode exhibits a high reversible capacity of 673 mA h g^{-1} at 0.1 A $g^{-1}$and remarkable rate capacity of 375 mA h g^{-1} at high current density of 5 A g^{-1}. This work provides a promising strategy to design and regulate anode materials for high-performance and even commercially available LIBs.

Results and discussion

To confirm the work function change of Fe_2N after Co doping, density functional theory (DFT) calculations were performed by using the generalized gradient approximation (GGA), where several doping amounts were chosen for comparison. **Figure 1**a depicts the molecular structure model of $Co_{0.1}$-Fe_2N@C while the pristine Fe_2N and $Co_{0.3}$-Fe_2N are shown in **Figure**

S1 (Supporting Information). And then the work functions of pristine Fe_2N, $Co_{0.1}$-Fe_2N, and $Co_{0.3}$-Fe_2N were obtained, as illustrated in Figure 1b-d. By incorporating Co atoms into Fe_2N, the work function of Co-doped Fe_2N exhibits an increase compared to pristine Fe_2N. Through the DFT calculations, we found that the introduction of Co doping induces modifications in the electronic structure of Fe_2N. Consequently, this leads to a reduction in the Fermi level and an increase in the work function (4.5 eV for iron and 5 eV for cobalt), ultimately resulting in an enhanced adsorption energy of lithium ions.

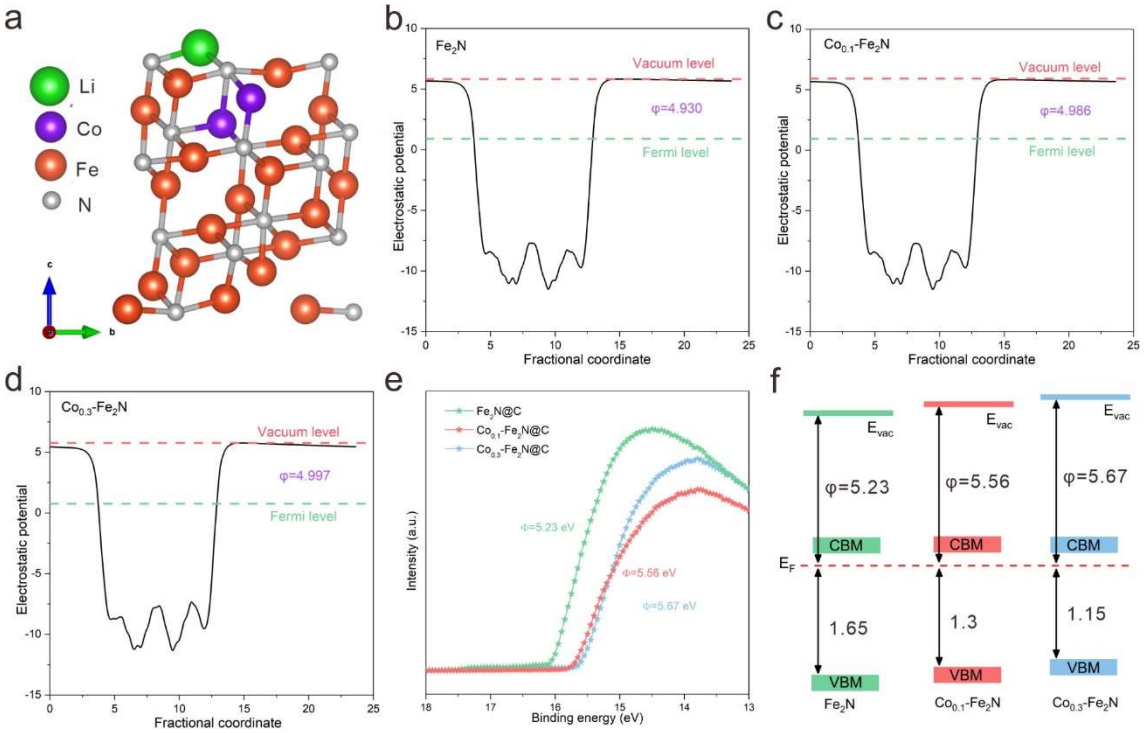

Figure 1. (a) molecular structure model of the $Co_{0.1}$-Fe_2N@C; (b-d) calculated work function of Fe_2N@C (b), $Co_{0.1}$-Fe_2N@C (c), and $Co_{0.3}$-Fe_2N@C (d); (e) Cutoff region of the UPS measurements from Fe_2N@C, $Co_{0.1}$-Fe_2N@C, and $Co_{0.3}$-Fe_2N@C; (f) Energy diagrams of the Fe_2N@C, $Co_{0.1}$-Fe_2N@C, and $Co_{0.3}$-Fe_2N@C.

Then, the pure Fe_2N and Co-doped Fe_2N were synthesized via a facile hydrothermal method (see details in the supporting information). Both the pure Fe_2N and Co-doped Fe_2N are uniformly distributed on the surface of honeycomb N-doped carbon foam. Based on the doping level, Co-doped Fe_2N with varying dopants is named Co_x-Fe_2N@C. To gain deeper insights into the electronic structures of Fe_2N@C, $Co_{0.1}$-Fe_2N@C, and $Co_{0.3}$-Fe_2N@C, we conducted an

analysis using ultraviolet photoelectron spectroscopy (UPS). Fe_2N@C, $Co_{0.1}$-Fe_2N@C, and $Co_{0.3}$-Fe_2N@C were transferred onto indium-tin oxide (ITO) conductive film glass ultraviolet photoelectron spectroscopy (UPS) measurements. The work function can be calculated from the difference between the cutoff energy and the photon energy of the exciting radiation. As shown in the cutoff region of Figure 1e, after Co doping, the work function of the Fe_2N is regulated from 5.23 eV to 5.56 eV. Moreover, the work function value is increased with the rising amount of dopant, implying a shift of the Fermi level toward VBM. This trend is consistent with the calculation results. Correspondingly, the energy diagrams of the Fe_2N@C, $Co_{0.1}$-Fe_2N@C, and $Co_{0.3}$-Fe_2N@C are illustrated in Figure 1f. In Figure 1f, it can be observed that the energy gap between the Fermi level and the valence band maximum (VBM) reduces from 1.65 eV to 1.3 eV, suggesting that Co doping lowers the Fermi level and enables electrons to be more readily excited from the VB to the CB, thus enhancing the electronic conductivity of the material. The iron in the iron nitride lattice can be substituted by cobalt atoms. This substitution can give rise to the additional holes in the lattice, thereby inducing a p-type doping effect. Since the doping of Co can greatly depleted the electron in the original Fe_2N, the electron concentration is significantly reduced, thus resulting in an enhanced work function. Adjusting the work function of Fe_2N can adjust the crystal structure, increase active sites, optimize adsorption energy, promote the rapid diffusion of lithium ions, and also contribute to the pseudocapacitance capacity.

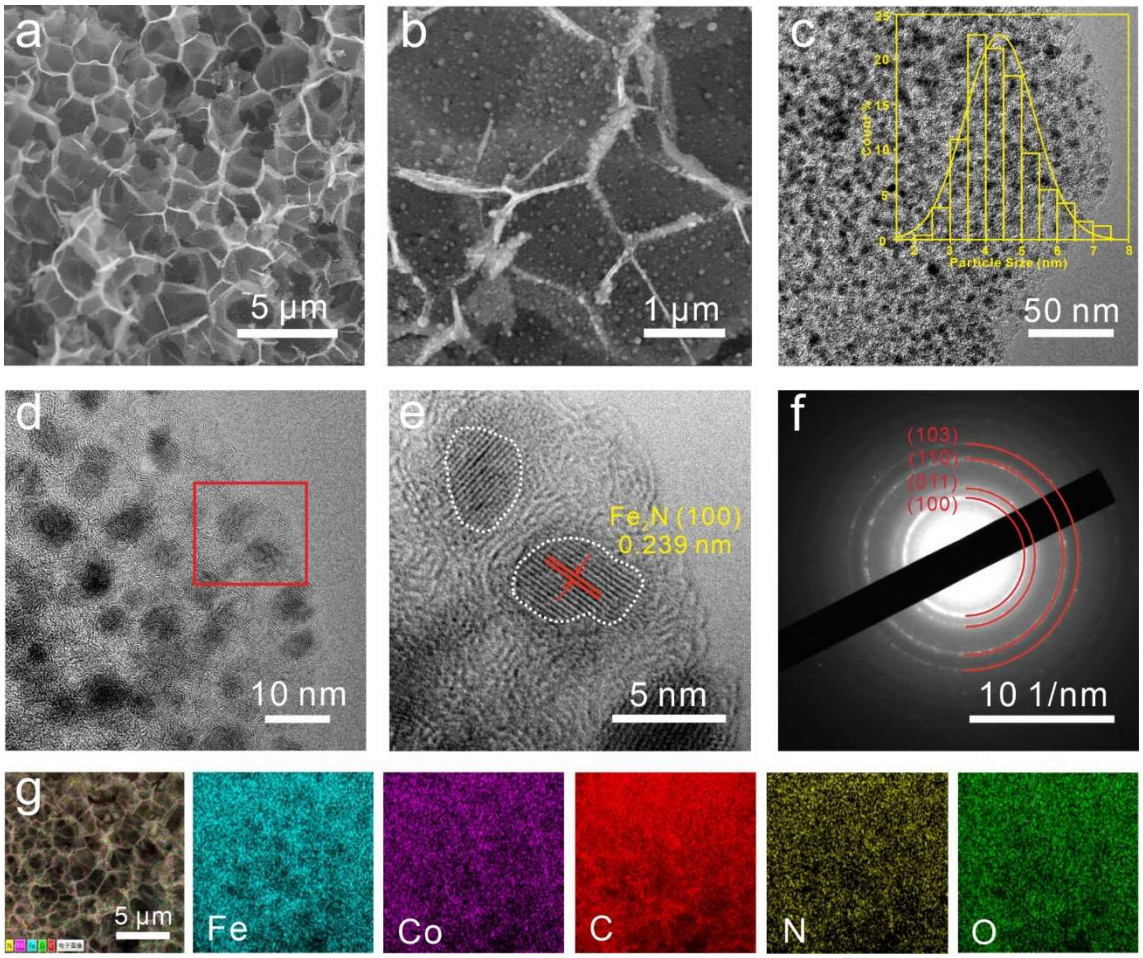

Figure 2. (a, b) SEM images of $Co_{0.1}$-Fe_2N@C under different magnifications; (c-f) TEM images and SAED pattern of $Co_{0.1}$-Fe_2N@C; (g) SEM image and the corresponding elemental mapping analysis of $Co_{0.1}$-Fe_2N@C.

Scanning electron microscopy (SEM) and transmission electron microscopy (TEM) were employed to identify the carbon structure and morphology. The SEM images of $Co_{0.1}$-Fe_2N@C under different magnifications are shown in **Figure 2**a, b. One can find that the Fe_2N nanoparticles are well-dispersed and uniformly anchoring on the surface of honeycomb carbon foam. Figure S2 (supporting information) displays the SEM pictures of the honeycomb carbon foam, Fe_2N@C, $Co_{0.05}$-Fe_2N@C, and $Co_{0.3}$-Fe_2N@C. It is evident that the particle size of Fe_2N increases with the rising amount of Co dopants. When it reaches 0.3, the $Co_{0.3}$-Fe_2N@C nanoparticles begin to aggregate into larger particles. Futher, the three-dimensional honeycomb carbon foam can effectively increase the specific surface area and conductivity and thereby

reduce aggregation of Fe_2N. The TEM image in Figure 2c shows the uniformly distributed $Co_{0.1}$-Fe_2N nanoparticles on the carbon layer with an average size of 3~6 nm. The high-resolution electron microscopy (HRTEM) images are shown in Figures 2d and 2e. The measured lattice d-spacing of $Co_{0.1}$-Fe_2N is 0.239 nm, corresponding to the (100) crystal plane of Fe_2N. On the edge of the $Co_{0.1}$-Fe_2N nanoparticles, the presence of amorphous carbon layers can also be confirmed by the HRTEM image. Then, the selected area electron diffraction (SAED) pattern was conducted and presented in Figure 2f. The clearly defined diffraction spots and rings correspond to the (011), (100), (110), and (103) crystal planes of Fe_2N. We additionally utilized the energy-dispersive spectroscopy (EDS) to clarify the elemental distribution and composition. Figure 2g reveals the uniform distribution of Co, Fe, N, O, and C elements, which confirms the successful doping of Co into Fe_2N. Table S1 also includes a list of the atomic ratios for the elements Co, Fe, N, O, and C.

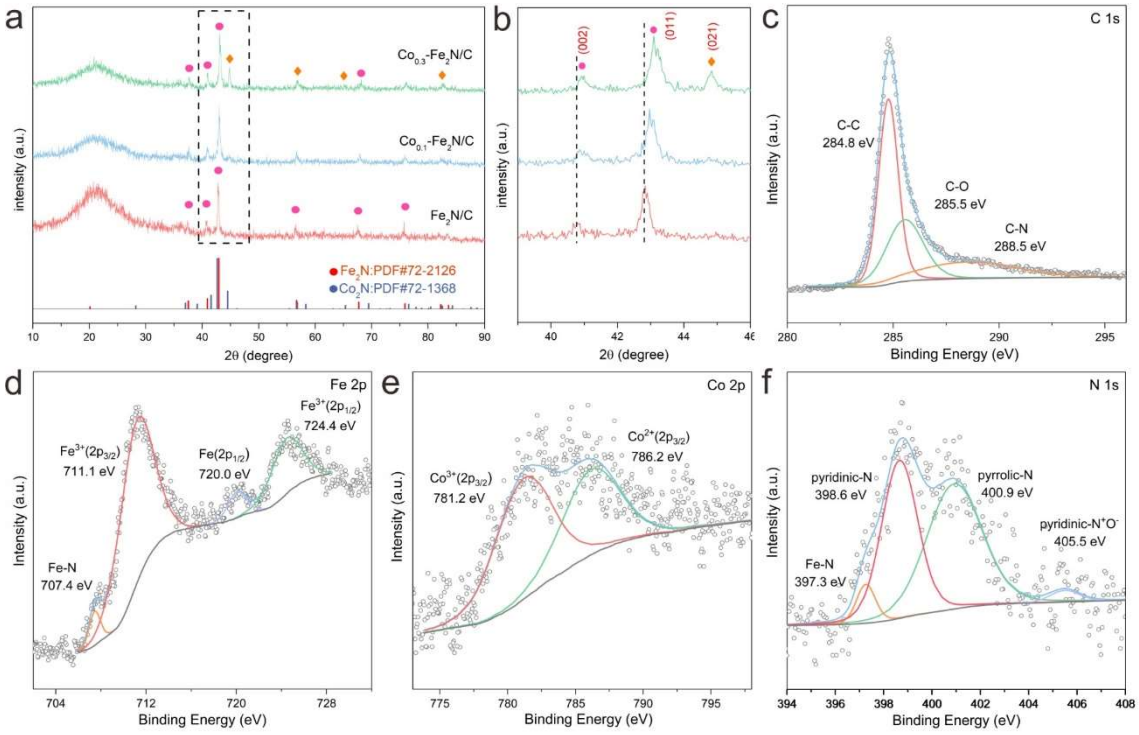

Figure 3. (a,b) XRD patterns of the Fe_2N@C, $Co_{0.1}$-Fe_2N@C, and $Co_{0.3}$-Fe_2N@C; (c) C 1s, (d) Fe 2p, (e) Co 2p, and (f) N 1s XPS spectra of $Co_{0.1}$-Fe_2N@C.

X-ray diffraction (XRD) pattern was performed to confirm the crystalization information and is presented in Figure 3a. It can be observed from Figure 3a that the XRD pattern of Fe_2N@C sample has an obvious strong diffraction peak at 2θ ≈ 42.94°, which corresponds to the (011) crystal face of Fe_2N. Moreover, the diffraction peaks at 2θ ≈ 40.89°, 56.70°, 67.72°, and 75.88° are also perfectly consistent with the standard card of Fe_2N (PDF#72-2126, space group *P3m1*, a = b = 2.76 Å, c = 4.41 Å). Fe_2N exhibits a face-centered cubic (fcc) structure in which Fe atoms form the fcc lattice of dots, and each Fe atom is surrounded by six N atoms, which occupy the octahedral interstitial positions. In the *P3m1* space group (hexagonal crystal system), the Fe atoms are located at the corner and face positions of the fcc lattice, while the N atoms are located at the center of the lattice. The XRD pattern of the $Co_{0.3}$-Fe_2N@C sample shows a strong diffraction peak at 2θ≈44.49°, corresponding to the (021) crystal face of Co_2N, which matches the standard card of Co_2N (PDF#72-1368), indicating that cobalt has been successfully doped into the Fe_2N@C composite. With the increase in cobalt doping content, $Co_{0.3}$-Fe_2N@C shows an obvious cobalt nitride characteristic peak. However, $Co_{0.1}$-Fe_2N@C does not show an obvious characteristic peak of cobalt nitride, which may be due to the low doping amount of cobalt, so XRD cannot detect the characteristic peak signal of cobalt nitride. Figure 3b shows a magnified region in which the patterns of the (011) and (002) planes shift to higher degrees as the Co dopants increase.This should be attributed to the introduction of Co into the Fe_2N crystal lattice, while the attendant is the lattice distortion. When the Co doping content reaches 0.3, one can observe the appearance of the Co_2N crystalline phase from the XRD pattern.

X-ray photoelectron spectrum (XPS) was employed to detect the surface chemistry of the $Co_{0.1}$-Fe_2N@C. Figure 3c shows the fitted C 1s fine spectrum at $Co_{0.1}$-Fe_2N@C. The prominent peak at 284.8 eV belongs to C−C, while the two peaks at 285.5 eV and 288.5 eV correspond to C−O and C−N bonds, respectively. As shown in Figure 3d, The Fe 2p XPS spectrum showed two strong peaks at 724.4 and 711.1 eV, corresponding to the Fe $2p_{1/2}$ and Fe $2p_{3/2}$ of Fe^{3+}

signals, respectively. And a small peak at 707.4 eV is attributed to Fe−N, confirming the presence of iron nitride. Therefore, the mixed valence states of Fe^{2+} and Fe^{3+} were confirmed in $Co_{0.1}$-Fe_2N@C. The Co 2p XPS spectrum, as seen in Figure 3e, revealed two prominent peaks at 781.2 and 786.2 eV, which corresponded to the Co $2p_{3/2}$ of Co^{3+} signals and Co $2p_{3/2}$ of Co^{2+} signals, respectively. This verified the mixed valence states of the Co^{3+} and Co^{2+}. Moreover, the N 1s XPS spectrum was deconvoluted into a metal nitride peak at 397.2 eV, which again confirms the presence of iron nitride. In addition, there is the presence of pyridine-N at 398.6 eV and pyrrole-N at 400.7 eV, corresponding to the N-doped carbon nanosheets (Figure 3f). From the fitting results of XPS, it can be seen that the proportion of Fe atoms is about 3.19%, the proportion of Co atoms is about 0.54%, and the ratio of Co (Fe+Co) is about 0.14, which is exactly close to the stoichiometric ratio in $Co_{0.1}$-Fe_2N@C. It shows that we have successfully prepared $Co_{0.1}$-Fe_2N@C. In addition, according to the TG measurement, it is calculated that the $Co_{0.1}$-Fe_2N content in $Co_{0.1}$-Fe_2N@C is 32wt% (Figure S3).

Such $Co_{0.1}$-Fe_2N@C nanoparticles thus exhibit at least the following multiple merits: (1) $Co_{0.1}$-Fe_2N@C particles are in the nanometer range, which reduces the volume effect; (2) The carbon layer is not only an electronic conduction network but also plays a role of dispersion and protection, ensuring the electrochemical activity of all nanoparticles; (3) The $Co_{0.1}$-Fe_2N@C nanoparticles in the framework are well-confined, allowing them to expand without being crushed. Then, the $Co_{0.1}$-Fe_2N@C nanoparticles were served as anode material for LIBs.

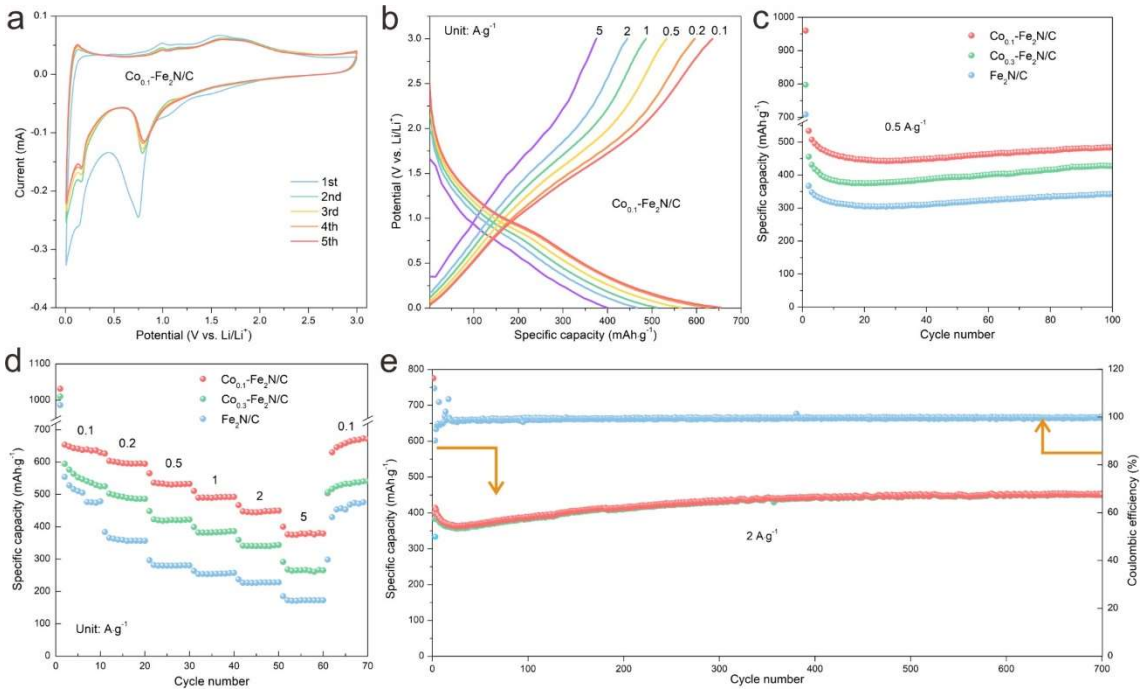

Figure 4. (a) Subsequent CVs of the $Co_{0.1}$-Fe_2N@C anode at a scan rate of 0.2 mV s^{-1}; (b) The galvanostatic charge/discharge curves of the $Co_{0.1}$-Fe_2N@C anode at different current densities; (c) constant current charge/discharge curves of Fe_2N@C, $Co_{0.1}$-Fe_2N@C, and $Co_{0.3}$-Fe_2N@C anodes at 0.5 A g^{-1} current density; (d) rate capability of Fe_2N@C, $Co_{0.1}$-Fe_2N@C, and $Co_{0.3}$-Fe_2N@C obtained at different current densities from 0.1 A g^{-1} to 5 A g^{-1}; (e) cycling stability and Coulombic efficiency of $Co_{0.1}$-Fe_2N@C at current density of 2 A g^{-1}.

Figure 4a shows the cyclic voltammogram (CV) curves of the $Co_{0.1}$-Fe_2N@C electrode for the first five cycles, which were tested between 0.01 and 3.0 V vs. Li^+/Li at a scan rate of 0.2 mV s^{-1}. The CV measurements of Fe_2N@C, $Co_{0.05}$-Fe_2N@C, and $Co_{0.3}$-Fe_2N@C anodes were also employed for comparision (Figure S4-S6). In the first discharge cycle, a pronounced cathodic peak at around 0.75 V was observed and disappeared in the subsequent cycles, which could be ascribed to the irreversible formation of SEI films, and the reduction of Fe_2N to Fe(0) nanoclusters dispersed in Li_3N matrix, followed the conversion reaction of $Fe_2N + 3Li^+ + 3e^- \rightarrow 2Fe + Li_3N$. The subsequent curves showed remarkable reproducibility with good overlapping of all the peaks at around 0.75 and 1.25 ~ 1.75 V, suggesting the high reversibility of the conversion reaction between Fe_2N and Fe(0). Figure 4b and S7-S9 show the charging and discharging curves of Fe_2N@C, $Co_{0.05}$-Fe_2N@C, $Co_{0.1}$-Fe_2N@C, and $Co_{0.3}$-Fe_2N@C

negative electrodes at different magnifications. The slightly tilted platform can be seen in the figure and varies little at different current densities. The negative electrode $Co_{0.1}$-Fe_2N@C showed the best electrochemical performance compared to the negative electrodes Fe_2N@C, $Co_{0.05}$-Fe_2N@C, and $Co_{0.3}$-Fe_2N@C. Under the applied current density, the voltage curve shows a clear plateau, which is the typical characteristic of the pseudocapacitive charge storage behavior of battery materials. The constant current curves of Co_x-Fe_2N@C anodes with different cobalt doping ratios were recorded at a current density of 0.5 A g^{-1} after five charge/discharge cycle activation (Figure 4c and Figure S10). The capacities of Fe_2N@C, $Co_{0.05}$-Fe_2N@C, $Co_{0.1}$-Fe_2N@C, and $Co_{0.3}$-Fe_2N@C anode materials at a current density of 0.5 mA h g^{-1} are 341.5, 428.6, 483.7, and 387.4 mA h g^{-1}, respectively. It can be seen that the $Co_{0.1}$-Fe_2N@C anode material has the highest capacity and the best charge and discharge performance. Moreover, the rate performance of $Co_{0.1}$-Fe_2N@C was investigated at current densities of 0.1, 0.2, 0.5, 1, 2, and 5 A g^{-1}, and the corresponding capacities were 654 (2nd cycle), 626 (12th cycle), 565 (22nd cycle), 510 (32nd cycle), 467 (42nd cycle), 400 (52nd cycle), and 671 mA h g^{-1} (72nd cycle) (Figure 4d and Figure S11), respectively. It can be seen that the $Co_{0.1}$-Fe_2N@C material has the highest capacity and the best charge and discharge performance. After abruptly switching the current density back to 0.1 A g^{-1}, high capacities could be fully restored for repeated stable cycling, indicating the excellent robustness and stability of the $Co_{0.1}$-Fe_2N@C electrode. Figure 4e shows that the $Co_{0.1}$-Fe_2N@C anode material can still maintain the high capacity of 451 mA h g^{-1} after 700 cycles at a current density of 2 A g^{-1}. In contrast, the specific capacity of the $Co_{0.1}$-Fe_2N@C electrode is significantly higher than that of the other electrodes, which indicates that the $Co_{0.1}$-Fe_2N@C negative electrode still exhibits the best long-cycle stability even when charged and discharged at high current density. It can be obviously observed that the specific capacity of the $Co_{0.1}$-Fe_2N@C electrode shows a slow growth trend after the activation of the first few cycles. This phenomenon of slow capacity growth is due to the fact that the transmission rate of lithium ions in the high current density cycle is much higher

than that in the low current density, which makes the ion unable to fully combine with the activity in the initial cycle, resulting in a low initial discharge specific capacity. In the subsequent cycle, lithium ions gradually bind to deeper sites. More discharge specific capacity is provided. At the same time, the discharge curve of $Co_{0.1}$-Fe_2N@C is very stable after 700 charge-discharge cycles, and the Coulomb efficiency is close to 100%, showing excellent long-cycle stability. The excellent electrochemical performance of the $Co_{0.1}$-Fe_2N@C electrode can be attributed to the improved electrical conductivity of this 3D honeycomb carbon layer structure, which shortens the transport path of Li^+ and electrolyte ions, while providing a high-speed channel for ion and electron transport. At the same time, the large specific surface area provides sufficient buffer space to alleviate the volume expansion effect of Fe_2N in the charging/discharging process. In addition, Co doping leads to the enhancement of Fe_2N in work function, which also increases its adsorption energy to Li^+ and accelerates the charge transfer, thereby boosting its cycling performance. In comparison with the literature (Table S2), the $Co_{0.1}$-Fe_2N@C anode material also exhibits superior cycling performance and stability.

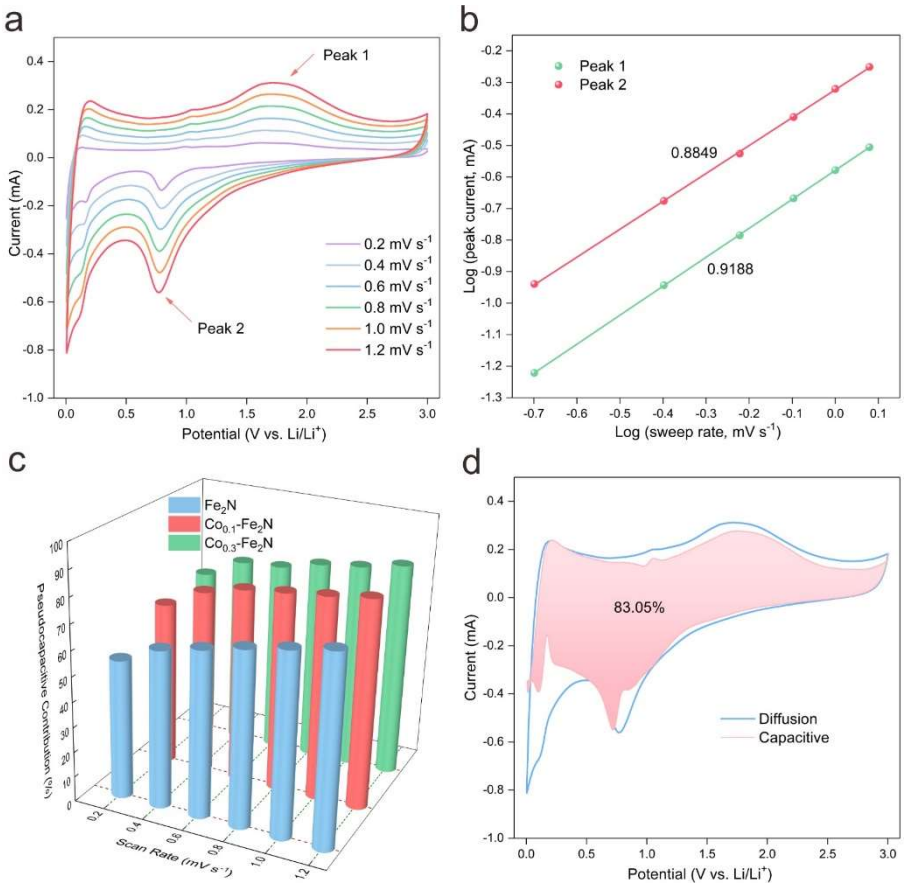

Figure 5. (a) The CV curves obtained at the scanning speed of 0.2 mV s^{-1}, 0.4 mV s^{-1}, 0.6 mV s^{-1}, 0.8 mV s^{-1}, 1.0 mV s^{-1}, and 1.2 mV s^{-1}, respectively; (b) corresponding log i versus log v plots at each redox peak (peak current: i, scan rate: v); (c) pseudocapacitive contribution of Fe_2N@C, $Co_{0.1}$-Fe_2N@C, and $Co_{0.3}$-Fe_2N@C electrode at different scan rates; (d) The CV curve measured a scan rate of 1.2 mV s^{-1} and corresponding pseudocapacitive contribution.

The electrochemical dynamics of the Fe_2N@C electrode were further analyzed via testing CVs at different scan rates from 0.2 to 1.2 mV s^{-1} (**Figure 5**a), which mainly present reduction peak 1 and oxidation peak 2. It is reported that the peak current (i) and scan rate (v) follow the rule of $\log i = b\log v + \log a$, in which a and b are variable constants. If b is close to 1, it indicates the domination of pseudocapacitance during the discharge/charge process; when b is close to 0.5, the electrochemical process is controlled by ionic diffusion. As shown in Figure 5b, the b values of the oxidation and reduction peaks are 0.9188 and 0.8849, respectively, both showing that the pseudapacitive process dominates during discharge/charge, which is conducive to the rapid storage of lithium ions. As the scanning rate increased from 0.2 mV s^{-1} to 1.2 mV s^{-1}, the

pseudocapacitance contribution of the negative electrode Fe_2N@C increased from 55.29% to 75.75%, and the pseudocapacitance contribution of the negative electrode $Co_{0.1}$-Fe_2N@C increased from 65.59% to 83.05%. The pseudocapacitance contribution of the negative electrode $Co_{0.3}$-Fe_2N@C increased from 67.89% to 85.2%, and the contribution rate of the pseudocapacitance increased gradually with the increase of the scanning rate (Figure 5c). The shaded part represents the portion of the specific capacity that is contributed by the pseudocapacitance, which accounts for 83.05% of the total area at a scan rate of 1.2 mV s^{-1}. This result indicates that the process of lithium ion storage is mainly a pseudocapacitive controlled process (Figure 5d).

As shown in Figure S12, the $Co_{0.1}$-Fe_2N@C anode has a larger Li^+ diffusion coefficient than the Fe_2N@C anode. This proves that the doping of cobalt effectively reduces the energy barrier of ion diffusion and improves the fast reaction kinetics of the $Co_{0.1}$-Fe_2N@C anode. To further demonstrate the good performance of this $Co_{0.1}$-Fe_2N@C anode, its resistances were determined by electrochemical impedance spectroscopy (EIS). The Nyquist plots of different loops at the charged states are composed of depressed semicircles in the high-frequency regions and straight lines in the low-frequency regions (Figure S13). The $Co_{0.1}$-Fe_2N@C anode has smaller charge-transfer resistance (R_{ct}) and Warburg impedance (W_s) after several charge/discharge cycles than the Fe_2N anode. These results confirm the good conductivity of the $Co_{0.1}$-Fe_2N@C anode, stemming from the carbon coating layer (Figure S14). Therefore, the $Co_{0.1}$-Fe_2N@C anode exhibits a facilitated charge transfer process, namely a reversible capacity and excellent cycling stability.

Conclusion

In summary, $Co_{0.1}$-Fe_2N@C nanoparticles on a three-dimensional honeycomb carbon layer structure have been utilized as an anode material for the construction of ultra-stable lithium-ion batteries. The assembled LIBs exhibits enhanced cycling stability and rate

performance. This is because this three-dimensional honeycomb carbon layer structure has an improved conductivity, accommodates the volume expansion, and accelerates the electron/ion transport during the sodiation/desodiation processes. After cobalt doping, the work function of the Fe_2N is tailored from 5.23 eV to 5.56 eV. The work function value rises in proportion to the doping level. The doping of cobalt can adjust the work function of the material. The increase in the material work function not only increases the charge transfer, but also increases the adsorption energy of the material for lithium ions, thus improving the performance of the anode material.Therefore, this work provides a promising approach to design and synthesize novel anode materials for the production of high-performance and even commercially available LIBs.

Supporting Information

Supporting Information is available from the Wiley Online Library or from the author.

Acknowledgements

This work was supported by National Natural Science Foundation of China (Nos. 22372127), Natural Science Foundation of Hubei Province (Nos. ZRM2023000271, 2023AFB608).

Conflict of Interest

The authors declare no conflict of interest.

Received: ((will be filled in by the editorial staff))

Revised: ((will be filled in by the editorial staff))

Published online: ((will be filled in by the editorial staff))

References

[1] Chen, J.; Wu, X.-J.; Yin, L.; Li, B.; Hong, X.; Fan, Z.; Chen, B.; Xue, C.; Zhang, H., One-pot Synthesis of CdS Nanocrystals Hybridized with Single-Layer Transition-Metal Dichalcogenide Nanosheets for Efficient Photocatalytic Hydrogen Evolution. *Angewandte Chemie International Edition* **2015,** *54* (4), 1210-1214.

[2] Lewis, N. S.; Nocera, D. G., Powering the planet: Chemical challenges in solar energy utilization. *Proceedings of the National Academy of Sciences* **2006,** *103* (43), 15729-15735.

[3] Li, R.; Zhang, F.; Wang, D.; Yang, J.; Li, M.; Zhu, J.; Zhou, X.; Han, H.; Li, C., Spatial separation of photogenerated electrons and holes among {010} and {110} crystal facets of $BiVO_4$. *Nature Communications* **2013,** *4* (1), 1432.

[4] Mu, L.; Zhao, Y.; Li, A.; Wang, S.; Wang, Z.; Yang, J.; Wang, Y.; Liu, T.; Chen, R.; Zhu, J.; Fan, F.; Li, R.; Li, C., Enhancing charge separation on high symmetry $SrTiO_3$ exposed with anisotropic facets for photocatalytic water splitting. *Energy & Environmental Science* **2016,** *9* (7), 2463-2469.

[5] Yu, H.; Xiao, P.; Wang, P.; Yu, J., Amorphous molybdenum sulfide as highly efficient electron-cocatalyst for enhanced photocatalytic H_2 evolution. *Applied Catalysis B: Environmental* **2016,** *193*, 217-225.

[6] King, L. A.; Zhao, W.; Chhowalla, M.; Riley, D. J.; Eda, G., Photoelectrochemical properties of chemically exfoliated MoS_2. *Journal of Materials Chemistry A* **2013,** *1* (31), 8935-8941.

[7] Liu, C.; Wang, L.; Tang, Y.; Luo, S.; Liu, Y.; Zhang, S.; Zeng, Y.; Xu, Y., Vertical single or few-layer MoS_2 nanosheets rooting into TiO_2 nanofibers for highly efficient photocatalytic hydrogen evolution. *Applied Catalysis B: Environmental* **2015,** *164*, 1-9.

[8] Liu, C.; Kong, D.; Hsu, P.-C.; Yuan, H.; Lee, H.-W.; Liu, Y.; Wang, H.; Wang, S.; Yan, K.; Lin, D.; Maraccini, P. A.; Parker, K. M.; Boehm, A. B.; Cui, Y., Rapid water disinfection using vertically aligned MoS2 nanofilms and visible light. *Nature Nanotechnology* **2016,** *11* (12), 1098-1104.

[9] Chang, K.; Hai, X.; Ye, J., Transition Metal Disulfides as Noble-Metal-Alternative Co-Catalysts for Solar Hydrogen Production. *Advanced Energy Materials* **2016,** *6* (10), 1502555.

[10] Voiry, D.; Yang, J.; Chhowalla, M., Recent Strategies for Improving the Catalytic Activity of 2D TMD Nanosheets Toward the Hydrogen Evolution Reaction. *Advanced Materials* **2016,** *28* (29), 6197-6206.

[11] Lui, C. H.; Frenzel, A. J.; Pilon, D. V.; Lee, Y. H.; Ling, X.; Akselrod, G. M.; Kong, J.;

Gedik, N., Trion-Induced Negative Photoconductivity in Monolayer MoS_2. *Physical Review Letters* **2014,** *113* (16), 166801.

[12] Chernikov, A.; Berkelbach, T. C.; Hill, H. M.; Rigosi, A.; Li, Y.; Aslan, B.; Reichman, D. R.; Hybertsen, M. S.; Heinz, T. F., Exciton Binding Energy and Nonhydrogenic Rydberg Series in Monolayer WS_2. *Physical Review Letters* **2014,** *113* (7), 076802.

[13] Ugeda, M. M.; Bradley, A. J.; Shi, S. F.; da Jornada, F. H.; Zhang, Y.; Qiu, D. Y.; Ruan, W.; Mo, S. K.; Hussain, Z.; Shen, Z. X.; Wang, F.; Louie, S. G.; Crommie, M. F., Giant bandgap renormalization and excitonic effects in a monolayer transition metal dichalcogenide semiconductor. *Nature Materials* **2014,** *13* (12), 1091-1095.

[14] He, K.; Kumar, N.; Zhao, L.; Wang, Z.; Mak, K. F.; Zhao, H.; Shan, J., Tightly Bound Excitons in Monolayer WSe_2. *Physical Review Letters* **2014,** *113* (2), 026803.

[15] Yang, S.; Gong, Y.; Zhang, J.; Zhan, L.; Ma, L.; Fang, Z.; Vajtai, R.; Wang, X.; Ajayan, P. M., Exfoliated Graphitic Carbon Nitride Nanosheets as Efficient Catalysts for Hydrogen Evolution Under Visible Light. *Advanced Materials* **2013,** *25* (17), 2452-2456.

[16] Niu, P.; Zhang, L.; Liu, G.; Cheng, H. M., Graphene-Like Carbon Nitride Nanosheets for Improved Photocatalytic Activities. *Advanced Functional Materials* **2012,** *22* (22), 4763-4770.

[17] Tongay, S.; Sahin, H.; Ko, C.; Luce, A.; Fan, W.; Liu, K.; Zhou, J.; Huang, Y.-S.; Ho, C.-H.; Yan, J.; Ogletree, D. F.; Aloni, S.; Ji, J.; Li, S.; Li, J.; Peeters, F. M.; Wu, J., Monolayer behaviour in bulk ReS_2 due to electronic and vibrational decoupling. *Nature Communications* **2014,** *5* (1), 3252.

[18] Liu, E.; Fu, Y.; Wang, Y.; Feng, Y.; Liu, H.; Wan, X.; Zhou, W.; Wang, B.; Shao, L.; Ho, C.-H.; Huang, Y.-S.; Cao, Z.; Wang, L.; Li, A.; Zeng, J.; Song, F.; Wang, X.; Shi, Y.; Yuan, H.; Hwang, H. Y.; Cui, Y.; Miao, F.; Xing, D., Integrated digital inverters based on two-dimensional anisotropic ReS_2 field-effect transistors. *Nature Communications* **2015,** *6* (1), 6991.

[19] Guo, J.; Yang, Y.; Yu, W.; Dong, X.; Wang, J.; Liu, G.; Wang, T., Synthesis of α-Fe_2O_3, Fe_3O_4 and Fe_2N magnetic hollow nanofibers as anode materials for Li-ion batteries. *RSC Advances* **2016,** *6* (112), 111447-111456.

[20] Huang, Y.; Liu, H.; Ling, C.; Chen, X.; Zhou, D.; Wang, S., Hydrogen Activation on the Promoted and Unpromoted ReS_2 (001) Surfaces under the Sulfidation Conditions: A First-Principles Study. *The Journal of Physical Chemistry C* **2015,** *119* (30), 17092-17101.

[21] Zhang, Q.; Tan, S.; Mendes, R. G.; Sun, Z.; Chen, Y.; Kong, X.; Xue, Y.; Rümmeli, M. H.; Wu, X.; Chen, S.; Fu, L., Extremely Weak van der Waals Coupling in Vertical ReS_2

Nanowalls for High-Current-Density Lithium-Ion Batteries. *Advanced Materials* **2016,** *28* (13), 2616-2623.